Atmospheric Boundary Layer height estimation from aerosol lidar: a new approach based on morphological image processing techniques

Gemine Vivone[1], Giuseppe D'Amico[1], Donato Summa[1], Simone Lolli[1,2], Aldo Amodeo[1], Daniele Bortoli[3,4], and Gelsomina Pappalardo[1]

[1]Consiglio Nazionale delle Ricerche, Istituto di Metodologie per l'Analisi Ambientale (CNR-IMAA), Tito (PZ), Italy
[2]Kent State University (Florence Campus), 800 E Summit St, Kent, OH 44240, USA
[3]ICT Institute of Earth Sciences and Dept. of Physics, School of Sciences and Technology and IIFA, Univ. of Évora, 7000-671 Évora, Portugal
[4]EaRSLab Earth Remote Sensing Laboratory, Univ. of Évora, 7000-671 Évora, Portugal

Correspondence: Simone Lolli (simone.lolli@imaa.cnr.it)

Abstract. The Atmospheric Boundary Layer (ABL) represents the lowermost part of the atmosphere directly in contact with the Earth surface. The estimation of its depth is of crucial importance in meteorology and for anthropogenic pollution studies. The ABL Height (ABLH) measurements are usually far from being adequate, both spatially and temporally. Thus, different remote sensing sources can be of great help in growing both the spatial and temporal ABLH measurement capabilities. To this aim, aerosol backscatter profiles are widely used as proxy to retrieve the ABLH. Hence, the scientific community is making remarkable efforts in developing automatic ABLH retrieval algorithms applied to lidar observations. In this paper, we propose a ABLH estimation algorithm based on image processing techniques applied to the composite image of the total attenuated backscatter coefficient. A pre-processing step is applied to the composite total backscatter image based on morphological filters to properly set-up and adjust the image to detect edges. As final step, the detected edges are post-processed through both mathematical morphology and an object-based analysis. The performance of the proposed approach is assessed on real data acquired by two different lidar systems, deployed in Potenza (Italy) and Evora (Portugal), belonging to the EARLINET network. The proposed approach has shown higher performance than the benchmark consisting of some state-of-the-art ABLH estimation methods.

1 Introduction

The Atmospheric Boundary Layer is the part of the troposphere that is directly or indirectly influenced by the Earth's surface (land and sea), and responds to gases and aerosol particles emitted at the Earth's surface and to surface forcing at time scales of less than one day. Forcing mechanisms include heat transfer, fluxes of momentum, frictional drag and terrain-induced flow modification. For this reason, the ABL exhibits a strong diurnal variability depending on the solar cycle (**??**). The ABL thermodynamic stability is of pivotal importance in regulating turbulence, convection and precipitation, other than affecting the Earth-atmosphere exchanges of heat, momentum, pollutants and moisture (**??**). Moreover, the underlying surface plays also a

crucial role for the ABL development: the marine boundary layer follows completely different processes with respect to the boundary layer over land, which in turn is influenced by the surface albedo because different surfaces respond differently to the solar heating (**?**). Another aspect that plays a role in shaping the boundary layer height is the orography: mountain (covered or not by snow) boundary layer height exhibits a very different behavior with respect to urban or rural flat environment.

25   The ABL is crucial in meteorology and its depth norms the available volume that the anthropogenic pollutants emitted at surface can occupy, affecting their concentration and consequently the air-quality. For this reason, extremely bad air pollution episodes often happen during winter at extra-tropical latitudes, when a high-pressure anticyclone is making the ABL shallower while an insufficient solar radiation is unable to trigger the convection and mixing. Instead, for tropical regions, the ABL depth is mostly related to the monsoon circulation (**???**). For all the previously cited reasons, the ABL height (ABLH) has

30   been recognized as a fundamental complex key meteorological variable to improve the aerosol dispersion forecast and re-analysis (**?**), i.e., accurate and dense ABLH measurements are needed to tackle air-quality related issues in highly urbanized environment and greater metropolitan areas, being this variable directly related to pollutant accumulation.

    Despite its fundamental importance, ABLH measurements are far from being adequate, both spatially and temporally. The unique officially accepted measurements at global scale are carried out in the frame of the World Meteorological Organization

35   (WMO) radiosounding global network. These measurements, highly concentrated within the most advanced Western countries in the Northern Hemisphere, are taken twice per day (00UTC and 1200UTC) without providing an adequate temporal coverage neither capturing the ABL diurnal cycle due to the different time zone (**??**). The different remote sensing techniques might be of great help in growing both the spatial and temporal ABLH measurement capabilities. The thermodynamic atmospheric variables, i.e., the temperature and humidity, or the atmospheric profile of the wind speed, the attenuated backscattering from

40   clouds and aerosols can be used as proxy to retrieve the ABLH from the vertically-resolved profiles taken by both active and passive remote sensing instruments as microwave radiometers, sodars, ceilometers and lidars. Those instruments are currently deployed in the E-PROFILE network and the Aerosols, Clouds and Trace Gases Research Infrastructure (ACTRIS). The single-wavelength lidar, among all the different previously cited remote sensing techniques, is an active remote sensing instrument that provides vertically-resolved profiles of the optical and geometrical aerosol properties at high spatial and temporal resolution.

45   From the observed attenuated aerosol backscatter profile it is possible to infer the ABLH. The scientific community, in the past decades, made remarkable efforts in developing automatic ABLH retrieval algorithms applied to lidar observations. In fact, besides the visual inspection (**?**) or simply setting up a threshold on the signal itself (**?**), several algorithms existing in literature are based on detecting the abrupt change in aerosol concentration at the top of the boundary layer to retrieve the ABLH from each single lidar profile. Traditionally, some algorithms are based on detecting the strong gradient of the first derivative of

50   the backscattered range corrected lidar signal profile (**??**), while other ones are based on the second derivative (**?**) or the first derivative of the logarithm (**?**). Some alternative algorithms propose variants based on detecting the gradient of the normalized signal (**?**), of its cubic root (**?**) or fitting the lidar ideal profile (**??**). If the cross-polarization channel measurement is available for the lidar instrument, the ABLH can be retrieved from the changes in the lidar depolarization ratio as showed in (**?**). (**?**) retrieved the ABLH identifying the maximum variance of the backscattered signal, while in other several studies the ABLH is retrieved

55   applying the wavelet covariance transform (WCT) to the lidar signal (**????**). (**?**) put in evidence that a strong link exists between

the wavelet transform and the gradient method. Other hybrid methods combine the wavelet approach with the image processing techniques (**????**) or pair the measured aerosol-backscatter lidar profile with models, e.g. multi-wavelength numerical model (**?**); stability dependent model of ABLH temporal variation (**?**). Recently, sophisticated algorithms that include very advanced techniques were proposed: (**?**) developed an algorithm based on tracking (pathfinder) that employs graph theory to track the diurnal evolution of the ABLH. (**?**) applied for the first time the Cluster Analysis (CA) to lidar measurements to obtain the ABLH. Another recent technology takes advantage of an Ensemble Kalman Filter (EKF) to trace ABLH evolution from ground-based lidar observations as shown in (**?**). A more detailed review with more information about advantages and drawbacks of the reported algorithms can be found in (**?**).

In this manuscript we present the development and validation of a new algorithm to continuously retrieve the ABLH from measurements taken at different permanent observational sites deployed in the frame of the European Aerosol Lidar Network (EARLINET) included in the ACTRIS research infrastructure (**?**). The new implemented algorithm is using a fully image-based methodology (2-D): instead of analyzing the lidar observations profile by profile, the retrieval takes into account also the temporal dimension (at very high resolution). The algorithm framework needs as input a statistically significant temporal collection of the total attenuated backscatter vertically-resolved profiles. The retrieval consists in applying to the composite image during the pre-processing phase the morphological operators and the edge detectors. Instead, during the post-processing phase, after applying the morphological filters again, the significant edges are extracted through an object-based analysis that is proven to be particularly successful in determining the ABLH. This proof-of-concept is a useful starting point to develop a central common strategy to produce high-quality and reliable ABLH retrieval in the frame of the Global Atmosphere Watch (GAW) Aerosol Lidar Observation Network (GALION; (**?**)) project of the WMO, which has as main objective to harmonize all the existing lidar and ceilometer networks. Indeed, the proposed approach is able, after a proper parameter tuning phase, to work with a huge variety of data addressing the task of the ABLH estimation even for data acquired by simpler networks or less advanced systems.

The manuscript is organized as follows. Sect. **??** is devoted to the presentation of widely used state-of-the-art methods to estimate the ABLH. In Sect. **??**, the proposed image processing based approach is described. Afterwards, the experimental results are shown in Sect. **??**. Finally, conclusions are drawn in Sect. **??**.

2   ABL Lidar Retrievals

This section is devoted to the description of widely used state-of-the-art techniques exploited to estimate the ABLH when lidar data are involved. One of these techniques follows aerosols and can be used for the study of the boundary-layer vertical structure and time variability. In particular, several approaches can be used to this aim, as detailed in Sect. **??**. The most common used methods rely on gradient detection techniques or the use of the wavelet covariance transform. In the following of this section, we will take into account these two main categories of algorithms that estimate the ABLH with a special focus on the two methods belonging to the benchmark exploited to assess the performance of the proposed morphological image-based approach.

2.1 Gradient-based for ABLH Estimation

90 There are several methods to determine the ABLH from lidar observations that are based on the assumption that aerosol is trapped within the ABL. Those methods find the height where the aerosol concentration abruptly decreases. This happens because the aerosol particles within the ABL can be used as proxy to study the boundary-layer vertical structure and time variability. In fact, aerosols uplifted after sunrise by convective mixing can act as efficient tracers for the atmospheric portion over which mixing occurs. Aerosols can also be dispersed out of the ABL during strong convective events or temporary breaks

95 of the entraiment zone. Thus, elastic backscattered signals from aerosol particles measured by lidar systems is one of the methods that can be used in comparison with others to determine the height and the internal structure of the ABL and, when possible, the residual layer and aerosol layers within and aloft the ABL (**?**).

For lidar systems, typically the detected backscattered light is much higher within the ABL than in the free troposphere due to the higher abundance of particles. The lidar equation is defined as:

$$P(\lambda, z) = P(\lambda_0, z)O(z)\frac{A}{z^2}\left[\beta_{par}(\lambda, z) + \beta_{mol}(\lambda, z)\right]T_{mol}(\lambda, z)T_{par}(\lambda, z) + P_{bgd}(\lambda), \tag{1}$$

where λ_0 and λ are the emitted and received lidar wavelength (laser wavelength), z is the vertical height, $O(z)$ is the overlap function, A refers to a system function (area and typical configuration), β_{mol} and β_{par} are the backscatter coefficients for molecular and particle components, respectively, T_{mol} and T_{par} indicate the atmospheric transmissivity and P_{bgd} is the background signal. Often it is preferred to use the corrected signal for the square of the quota, named range corrected signal (RCS),

105 defined as:

$$P_{rcs}(\lambda, z) = \left[P(\lambda, z) - P_{bgd}(\lambda)\right]z^2 \tag{2}$$

In order to determine an estimate of the height of ABLH, we directly apply the derivative method exploiting the logarithm of the quantity (**??**). In this case, the lidar elastic backscatter signal, $P(\lambda, z)$, is used. Thus, we have that the ABLH, $H(\lambda)$, can be obtained as follows:

$$H(\lambda) = \min_z\left\{\frac{d}{dz}\log\left[P_{rcs}(\lambda, z)\right]\right\}. \tag{3}$$

The minimum of the quantity in (**??**) identifies the transitions between different layers, and the absolute minimum identifies the height of the boundary layer, because the largest variation of the lidar signal is considered corresponding to the largest variation of the aerosol concentration. This is only valid under scenarios of no decoupled layers. $H(\lambda)$ represents the transition from the stable layer to a neutral or unstable condition above. The method has been applied to the maximum vertical spatial

115 and temporal resolutions.

2.2 Wavelet Covariance Transform for ABLH Estimation

The Wavelet Covariance Transform (WCT) is defined as (**?**)

$$c(b) = \frac{1}{a}\int_{z_b}^{z_t} s(z)h\left(\frac{z - b}{a}\right)dz, \tag{4}$$

where $s(z)$ is the range-corrected lidar backscatter signal, z is the measurement height, z_b and z_t are the lower and upper limits of the lidar return signal profile, respectively, a is the dilation factor, b the translation, and h is defined as the Haar wavelet function, i.e.

$$h(x) = \begin{cases} 1, & \text{if } -\frac{1}{2} \le x \le 0 \\ -1, & \text{if } 0 < x \le \frac{1}{2} \\ 0, & \text{otherwise.} \end{cases} \tag{5}$$

In order to have a more efficient implementation and to gain more insights about WCT, (**??**) can be seen as convolution. Thus, starting from (**??**) we have:

$$c(b) = \int_{-\infty}^{+\infty} s(z) w(b - z) \, dz = s(b) * w(b) \tag{6}$$

where

$$w(x) = \frac{1}{a} h\left(-\frac{x}{a}\right), \tag{7}$$

$*$ stands for the convolution operator and z_b and z_t are set to $-\infty$ and $+\infty$, respectively, without harming the generality. It is worth to be pointed out that the Haar function $h(x)$ in (**??**) can be rewritten using the derivative and a triangular window. Hence, we have that:

$$h(x) = \frac{1}{2} \frac{d}{dx} \Lambda(2x), \tag{8}$$

where

$$\Lambda(x) = \begin{cases} 1 + x, & \text{if } -1 \le x \le 0 \\ 1 - x, & \text{if } 0 < x \le 1 \\ 0, & \text{otherwise} \end{cases} \tag{9}$$

is the triangular window.

Let us consider the Fourier transform of $c(b)$ in (**??**), where b plays the role of the time domain in the classical Fourier analysis for linear time-invariant (LTI) systems. The convolution in time can be seen in the transformed domain as (**?**):

$$C(f) = S(f)W(f), \tag{10}$$

where $C(f) = \mathcal{F}[c(b)]$, $S(f) = \mathcal{F}[s(b)]$, $W(f) = \mathcal{F}[w(b)]$, and $\mathcal{F}[\cdot]$ is the forward Fourier transform. Considering the derivative and the scaling properties of the Fourier transform (**?**) and that the dilation $a \ge 0$, after simple algebra, starting from (**??**) and (**??**) we have that:

$$W(f) = \mathcal{F}[w(b)] = i\frac{\pi}{2} f \, sinc^2\left(\frac{a}{2} f\right) \tag{11}$$

where i is the imaginary unit and

$$sinc(x) = \frac{\sin(\pi x)}{\pi x} \tag{12}$$

is the normalized sine cardinal function.

Now if we consider the modulus of $C(f)$, i.e., $|C(f)|$, in (??), we have that $|C(f)| = |S(f)||W(f)|$, where the modulus of $W(f)$ is

$$|W(f)| = \frac{\pi}{2}|f|\,sinc^2\left(\frac{a}{2}f\right). \tag{13}$$

Thus, it is easy to see that if $f \to \pm\infty$, $|W(f)| \to 0$ and if $f = 0$, $|W(f)| = 0$. Indeed, the Fourier transform of the triangular window in (??) can be seen as a low-pass filter with a cut-off depending on a (i.e., the factor in (??) represented by the $sinc^2$ function). Instead, the derivative in (??) leads to a multiplication by $|f|$ in (??) generating a band-pass filter with cut-off frequencies depending on a, which rules the selection of a portion of the whole frequency spectrum. Hence, we have from (??) that higher frequencies of $s(b)$ are passed with respect to the low-pass filter defined by the triangular windows. In this sense, the WCT method with the Haar wavelet function can be considered as a particular gradient-based method.

In all the equations above, we neglected the dependence on a of the WCT c. Indeed, the dilation a is set to a fixed value. A rule of thumb can be found in (?). However, in this paper, in order to have a high performance method for our benchmark, we set a to its optimal value (which is sensor-dependent) obtained via a grid search approach. Furthermore, following the indications in (?), we normalize the range-corrected signal by its maximum value found below a given height (usually set around 1000 m). The normalization guarantees the applicability of a unique threshold (set to 0.05 as suggested in (?)) on $c(b)$ in order to find the ABL even at very different backscatter conditions in rather clean or very polluted air.

3 The Proposed Morphological Image Processing Approach (MIPA)

The composite image on which the proposed algorithm is applied consists in the temporal sequence of the range-corrected vertically-resolved acquired lidar profiles. The proposed MIPA algorithm has no prior knowledge on ABLH and the image processing approach relies on: i) a block that reduces the vertical spatial resolution to reach a working spatial resolution around 20m if the spatial resolution of the system is finer; ii) a pre-processing step applied to the daily lidar data exploiting mathematical morphology; iii) Canny's edge detection (?) applied to the pre-processed data; iv) a post-processing starting from the detected edges and based on both mathematical morphology and an object-based analysis to get the final outcome. In the following sections, the basics of morphological operators are presented first. Then, the proposed MIPA algorithm will be detailed.

3.1 Basics of Morphological Operators

An image $\mathbf{I}$: $E \subseteq \mathbb{Z}^2 \to V \subseteq \mathbb{Z}$ is analyzed by morphological operators via the so-called structuring element (SE), here denoted as B (?), which can be defined through its spatial support $N_B(\mathbf{x})$ (i.e., the neighborhood with respect to the position $\mathbf{x} \in E$ in

which B is centered) and by its values. For *flat SEs* (i.e., SEs with unitary values), the only free parameters are the origin and N_B. We will focus on these SEs in this work.

Erosion, $\varepsilon_B[\mathbf{I}]$, and *dilation*, $\delta_B[\mathbf{I}]$, are the two basic operators defined, for each $\mathbf{x} \in \mathbf{I}$, as follows:

$$\varepsilon_B[\mathbf{I}](\mathbf{x}) = \bigwedge_{\mathbf{y} \in N_B(\mathbf{x})} \mathbf{I}(\mathbf{y}), \tag{14}$$

$$\delta_B[\mathbf{I}](\mathbf{x}) = \bigvee_{\mathbf{y} \in N_B(\mathbf{x})} \mathbf{I}(\mathbf{y}), \tag{15}$$

where $\bigwedge_S$ and $\bigvee_S$ are the infimum and supremum values in the set S, respectively.

The erosion (respectively dilation) application has as filtering effect that suppresses bright (respectively dark) regions smaller than B and the enlargement of dark (respectively bright) ones. For bright and dark regions we mean that the local contrast in a certain region has intensity values greater or lower with respect to the surrounding ones, respectively. Erosion and dilation operators can be recast into minimum and maximum operators on B, respectively, if $\mathbf{I}$ is a binary image.

We also introduce for convenience the *opening* and *closing* that correspond to the two possible sequential compositions of erosion and dilation. In particular, the *opening* is defined as:

$$\gamma_B[\mathbf{I}] = \delta_{\breve{B}}[\varepsilon_B[\mathbf{I}]], \tag{16}$$

where $\breve{B}$ denoting the SE obtained by reflecting B with respect to its origin. Instead, the *closing* is given by

$$\phi_B[\mathbf{I}] = \varepsilon_{\breve{B}}[\delta_B[\mathbf{I}]]. \tag{17}$$

A closing removes dark regions smaller than B, whereas an opening suppresses bright ones. For further details about morphological operators, the interesting readers can refer to the related literature (**?**).

A number of morphological operators can be obtained by properly combining the above-mentioned operators. Two instances, which are of great interest in this work, are represented by the residuals of the application of erosion and dilation, usually called *internal gradient* and *external gradient*, respectively (**?**). In particular, the *internal gradient*, $\rho_B^-[\mathbf{I}]$, is defined as

$$\rho_B^-[\mathbf{I}] = \mathbf{I} - \varepsilon_B[\mathbf{I}], \tag{18}$$

and the *external gradient*, $\rho_B^+[\mathbf{I}]$, is given by

$$\rho_B^+[\mathbf{I}] = \delta_B[\mathbf{I}] - \mathbf{I}. \tag{19}$$

These two gradients are also often called *Half-Gradients* (HGs).

In the remaining of this section, the four modules that constitutes the proposed approach will be detailed.

3.2 Profile Resolution Reduction

This first block starts from a matrix $\mathbf{I}\colon E \subseteq \mathbb{Z}^2 \to V \subseteq \mathbb{Z}$ that is the daily sequence of the attenuated backscatter profiles. These latter form the columns of $\mathbf{I}$. Thus, the number of rows is related to the maximum height and the spatial resolution of the

system, instead the number of columns is about its temporal resolution. The downsampling with a factor R, which aims to reduce the bins' spatial resolution, is implemented by a low-pass filter along each column of $\mathbf{I}$ plus decimation with a factor R. In particular, a moving-average filter is simply applied as low-pass filtering. The support (i.e., the length of the sliding window) of the filter is R, again. Thus, R is the unique tuning parameter that is selected in order to have a spatial resolution not finer than 20 m. This value has been empirically set in order to avoid multiple edges corresponding to the same layer, thus having sharper and uniquely identifiable edges. Hence, R can be directly calculated from the system's spatial resolution bringing the initial product to the target spatial resolution. This operation is performed to have a sharper edge defining the ABL. The outcome is an image $\mathbf{I}_D$ used as input in the pre-processing step. It is worth to be remarked that if we work with data having a spatial resolution coarser than 20 m, R is set to one, thus skipping this step implying that $\mathbf{I}_D$ is equal to $\mathbf{I}$.

3.3 Pre-processing Based on Mathematical Morphology

In this work, we propose the use of a low-pass filter based on HGs to pre-process $\mathbf{I}_D$. Before coming into the details of the used operator, let us define the complement of a generic operator Ψ, i.e., $\overline{\Psi}$, as $\overline{\Psi} = id - \Psi$, where id is the identity operator. It is worth to be remarked that when discontinuities are present both the HGs assume positive values constituting an approximation of the norm of the signal gradient (**?**). Thus, the difference of the two (internal and external) HGs represents a detail extraction operator, since it reproduces the variations of the function with respect to the local mean (**?**). This operator exploiting a SE B_{pre}, denoted as $\overline{\Psi}_{HG,B_{pre}}$, is defined as follows:

$$\overline{\Psi}_{HG,B_{pre}} = 0.5\left(\rho^- - \rho^+\right) \tag{20}$$

$$= 0.5\left(id - \varepsilon_{B_{pre}}\right) - 0.5\left(\delta_{B_{pre}} - id\right), \tag{21}$$

in which the factor 0.5 is applied to preserve the property of approximating the image gradient norm. The corresponding low-pass filter is simply given by the complementary operator of $\overline{\Psi}_{HG,B_{pre}}$, i.e.

$$\Psi_{HG,B_{pre}} = id - \overline{\Psi}_{HG,B_{pre}} \tag{22}$$

$$= id - \left[0.5(id - \varepsilon_{B_{pre}}) - 0.5(\delta_{B_{pre}} - id)\right] \tag{23}$$

$$= 0.5\left(\varepsilon_{B_{pre}} + \delta_{B_{pre}}\right), \tag{24}$$

which corresponds to the semi-sum of the dilation and erosion operators. This operator is used in the pre-processing phase applying it to $\mathbf{I}_D$ and fixing B_{pre} to a *line SE* in the horizontal direction (i.e., along the time direction) with a length l_{pre}. It enables us to smooth the lidar image along the horizontal axis (where the dynamic of the ABL is quite slow), directionally reducing the noise and preserving the vertical edges that will be of crucial importance for the next step. The resulting image after pre-processing the image $\mathbf{I}_D$ is indicated as $\mathbf{I}_{pre}$ and it represents the input of the edge detection block.

3.4 Edge Detection

This processing step can be implemented in several ways. Every edge detector can be exploited to extract a first estimation of the ABL starting from $\mathbf{I}_{pre}$. Thus, the proposed approach is flexible and this block can be changed to possibly improve

the results. Approaches, already discussed in this paper, as Wavelet Covariance Transform (WCT) or gradient-based could be adopted. However, the analysis of the performance varying these strategies in the proposed framework is out-of-the-scope of this paper. Thus, we employed Canny's edge detector (the classical version available in commercial software as MATLAB) (**?**) to get the first estimation of the edge map, denoted as $\mathbf{E}$. The detected edges in $\mathbf{E}$ are indicated with 1, instead, the rest of the map (background) is labeled as 0. All the bins labeled as 1 in the edge map are potential candidates to represent the ABL.

3.5 Post-processing

After applying Canny's edge detector to the pre-processed data, the edge map $\mathbf{E}$ is analyzed by using further signal processing. In particular, morphological filters are exploited first. Then, a final post-processing phase relied upon an object-based analysis is performed. The two steps will be detailed in the following.

3.5.1 Post-processing Based on Morphological Operators

The post-processing based on morphological filters is applied to the edge map $\mathbf{E}$. This processing step is about removing unrealistic edges (i.e., edges that vary too fast with respect to the dynamic of the ABL). Thus, we apply a series of directional Low-Pass (LP) morphological filters. In particular, the used filters are obtained by sequentially applying an opening and a closing operator using the same structuring element B_{post}, i.e.

$$\overline{\Psi}_{LP,B_{post}} = \phi_{B_{post}} \gamma_{B_{post}}, \tag{25}$$

where B_{post} is a *line SE* with a length l_{post} and an angle θ. The application to $\mathbf{E}$ of these directional filters varying θ from θ_{min} to θ_{max} and combining the outputs with a maximum operator provides the output of this post-processing step, indicated as $\mathbf{E}_{post}$.

3.5.2 Object-based Post-processing

The object-based post-processing is applied to the edge map $\mathbf{E}_{post}$. The detected edges are indicated with 1, instead, the rest of the map (background) is labeled as 0. The first layer in $\mathbf{E}_{post}$ consists of the first (starting from the ground) bins detected as "edge" (i.e., labeled as 1) analyzing the edge map for each profile (*i.e.*, in the vertical direction).

We work on these edges extracting objects. The main concept is the use of the *connectivity* in an edge map, i.e., the way in which the bins labeled as "edge" (which assume value 1 in the edge map) are spatially related to their neighbors. A bin declared as "edge" is said "8-connected" if exists at least a bin belonging to its 8-neighborhood, i.e., the adjacent bins in vertical, horizontal, and diagonal directions, declared as "edge", as well. All the bins that are "8-connected" to each other form an object.

Thus, several objects, clustering the bins declared as "edge", are collected and analyzed. In particular, an analysis about the spatial variability of these objects is performed. Indeed, if the absolute Euclidean distance between the mean of the heights for each extracted object (using the connectivity procedure explained above) and the related mean calculated on the objects in its

Algorithm 1 The proposed ABL estimation algorithm.

- Reduce the profile resolution of $\mathbf{I}$ by a factor R to get $\mathbf{I}_D$

- Pre-process $\mathbf{I}_D$ by low-pass filtering using HGs, see (**??**), as described in Sect. **??**, to get $\mathbf{I}_{pre}$

- Estimate the edges of $\mathbf{I}_{pre}$ using Canny's edge detector obtaining the edge map $\mathbf{E}$

- Post-process the edge map $\mathbf{E}$, as described in Sect. **??**, using directional morphological filters as in (**??**) and the object-based analysis as described in Sect. **??**, in order to get $\mathbf{E}_{out}$

neighborhood exceeds a threshold δ_{post}, this object is removed from the solution. Finally, the outcome, i.e. the estimated ABL denoted as $\mathbf{E}_{out}$, is obtained by linearly interpolating the remaining objects in the edge map.

3.6 Overview of the Proposed MIPA Algorithm

265   Fig. **??** depicts the flowchart of the proposed MIPA approach. Instead, Algorithm **??** summarizes the sequence of the adopted signal processing steps in order to provide to the readers a complete overview of the proposed approach.

4   Results

This section describes the results obtained by applying the ABL detection algorithms detailed in the previous sections on several high-resolution total attenuated backscatter lidar timeseries. In particular, as we use the aerosol as proxy to determine the

270 ABLH, we considered observations at a longer wavelength (1064 nm) to get a higher contrast among the particle and molecular contribution. In order to show the robustness of the proposed methodology, we selected different case studies characterized by different atmospheric conditions in terms of both aerosol loading and solar background. Further, we applied MIPA on observations from two quite different multi-wavelength sensors operating in different sites in terms of topography: the Potenza lidar system MUSA and the Evora lidar system PAOLI.

275   MUSA is one of the reference lidar systems in the frame of EARLINET deployed at CNR-IMAA Atmospheric Observatory (CIAO) in Potenza (40.60N, 15.72E, 760 m asl). The lidar instrument is equipped with 3 elastic channels at 355, 532 and 1064 nm and 2 anelastic N2 Raman channels at 387 and 607 nm (**?**). Two independent polarization components of the elastic channel at 532 nm are separately detected in order to measure the particle depolarization ratio (**?**). All channels have a raw vertical resolution of 3.75 m and, except for the 1064 nm where only analog detection is used, all the channels are acquired

280 both in analog and photoncounting mode to enhance the detectable dynamic range. The typical raw time resolution is 60 s. The full overlap height of the MUSA lidar is around 250-300 m.

  PAOLI is the Evora EARLINET lidar system (38.57N, -7.91E, 293 m asl) and it operates 3 elastic channels (at 355, 532 and 1064 nm) and two anelastic channels at 387 and 607 nm (**?**). The total and the cross polarization channels at 532 nm are detected separately. Only photoncounting detection mode is used for all the channels. The raw vertical resolution is 30 m and

285 the time resolution is 30 s. The full overlap height of the PAOLI system is around 750-800 m.

Even if MUSA and PAOLI operate at the same wavelengths, their technical characteristics are very different: laser source, telescope, detection and acquisition system, space and time resolution, full overlap region. Moreover, the two lidars operate in locations that from topographic point of view are quite different one from the other. As a consequence, applying MIPA algorithm on both systems is a good benchmark to evaluate the algorithm performances.

MIPA algorithm uses as input the composite plot of the vertically-resolved attenuated backscattering coefficient at 1064 nm. High spatial and temporal resolution is needed to increase sensibility in using the directional morphological filter while long and continuous time series are needed to improve the accuracy in mapping the detected edges. The proposed case studies are continuous multi-day observations from MUSA and PAOLI lidar systems. in July 2012, during the EARLINET 72 hours exercise (**?**), both Evora and Potenza EARLINET lidar stations performed continuous measurements during 72 hours as proof of concept to demonstrate that EARLINET lidar network can provide aerosol optical products in NRT as operational service. The observations were automatically analyzed in NRT by the EARLINET Single Calculus Chain (SCC) (**?**), a common algorithm developed to centrally analyze and retrieve aerosol optical, geometrical and microphysical properties from the different EARLINET lidar instruments. The results obtained by applying the ABLH detection algorithm on both Potenza and Evora 72h datasets are described in Sect. **??**. Additionally, we selected further 3 Potenza cases described in Sect. **??**.

The total attenuated backscatter can be easily expressed in terms of measured lidar signals taking into account (**??**) and (**??**):

$$\beta_{att}(\lambda, z) = [\beta_{mol}(\lambda, z) + \beta_{par}(\lambda, z)] T_{mol}^2(\lambda, z) T_{par}^2(\lambda, z) = K P_{rcs}(\lambda, z) \tag{26}$$

where K is a calibration constant determined by imposing that $\beta_{att}(\lambda, z) = \beta_{mol}(\lambda, z) T_{mol}^2(\lambda, z)$ in an aerosol-free atmospheric region. It is important to note that morphological filter techniques rely only on the correlation among adjacent lidar range bin and not on their absolute numeric values. As a consequence, the ABLHs computed by the proposed MIPA algorithm are rather insensitive to the accuracy of the calibration constant K. Actually, the morphological algorithm can be applied to the range corrected signal (P_{rcs}) time series instead of the total attenuated backscatter one, providing the same results in terms of ABLH. This is in general not true for the traditional ABLH retrieval algorithms (derivative, WCT) where proper thresholds on absolute signal value need to be defined. Tab. **??** summarizes all the input parameters exploited by the compared approaches for the two lidar systems considered. These have been defined after a tuning phase on different lidar scenarios. It is worth to be remarked that the derivative approach requires no parameter to be set working on datasets at full resolution (60 s and 3.75 m for MUSA, 30 s and 30 m for PAOLI).

All the input data sets considered in the study have been previously pre-processed at high resolution by using the EARLINET SCC. In particular, starting from raw lidar data, several instrumental corrections (like for example trigger delay correction, dead time correction, analog and photoncounting signal glueing, etc.) and all the required raw signal handlings (like atmospheric background subtraction, range correction) have been applied. More details on the pre-processing procedure implemented in the EARLINET SCC are described in (**?**).

To asses the performance of all the considered ABLH retrievals, a reference needs to be set. As the most rigorous definition of the ABL is the one based on thermodynamic effects, we assume as reference for the ABLH the values retrieved from

320 atmospheric temperature and pressure profiles. In particular, the reference ABLHs described in (?) are derived applying on potential temperature defined as:

$$\theta(z) = T(z)(Ps_0/Ps(z))^k, \tag{27}$$

where $\theta(z)$ is the potential temperature that is function of the vertical height, z, Ps_0 is the atmospheric standard pressure (i.e., 1013.25 hPa), $T(z)$ is the temperature in kelvin degrees, $Ps(z)$ is the pressure that is function of z and $k = 0.286$. The tempera-
325 ture and pressure data are obtained from ECMWF models. It is important to note that, in general, the thermodynamic definition of the ABL is different from the one typically adopted in lidar-based observations, where the atmospheric aerosol is assumed to act as ABL tracer. During daytime conditions, the two definitions are typically equivalent: the ABL is well developed from a thermodynamic point of view and most of the aerosols are well mixed and trapped in it. During nighttime conditions, ABL can be composed of stable and residual layers. Consequently, the ABLH retrieved assuming the thermodynamic or the lidar-based
330 ABL definition can differ providing, in one case, the top of the stable and, in the other case, the top of the residual layer. In this context, it is worth to be underlined that the definition of the ABLH based on aerosol contents (the one commonly used in the lidar community) is somehow ambiguous because it is mainly based on the retrieval of the first (from the surface) edge in the profile of the lidar variable proportional to the aerosol contents. How this edge is attributed to a specific internal ABL sublayer cannot be determined without additional information such as turbulence or temperature.

335 The sounding data available for all the measurement dates considered in this study are quite few and except from one case they are not co-located with the lidar station. In particular, there are no sounding data available for Potenza for any of the 72h exercise day. The closest sounding stations are Brindisi (40.66N, 17.96E, 15 m asl and located about 180 km away from Potenza EARLINET station) and Pratica di Mare (41.67N, 12.45E, 32 m asl located about 300 km away from Potenza EARLINET station) which are both coastal sites with very different atmospheric conditions with respect to the mountain
340 Potenza lidar station (760 m asl). As a consequence, the corresponding temperature and pressure profiles cannot be used to retrieve a reliable ABLH reference. Only for one of the additional selected Potenza measurement case (November 20, 2014), a single radiosounding launched at CIAO observatory (?) is available, which however provides only one reference point that is not enough to well assess the performances of the lidar-based ABLH retrieval. For Evora EARLINET observational site, the closest sounding station is Lisboa/Gago Coutinho (38.77N, -9.13E, 110 m asl and located about 110 km away from Evora EARLINET
345 station) at noon local time daily. Even if in this case the atmospheric conditions characterizing Lisboa/Gago Coutinho sounding station could be considered similar to the ones characterizing the Evora EARLINET station, the 72h exercise ABLH reference points obtainable by using close soundings are only three and all referring to the same hour of the day.

Because of the lack of enough co-located and simultaneous soundings to guarantee a reliable ABLH reference for both Potenza and Evora measurement sites, the performance of the ABLH retrievals based on lidar observations has been assessed
350 comparing against the ABLH calculated using atmospheric temperature and pressure profiles as provided by the Numerical Weather Prediction (NWP) model. To our knowledge, NWP is the best alternative to the use of sounding data. In particular, to calculate the ABLH reference points for all the Potenza cases, we have used the high-resolution NWP provided by the ECMWF Integrated Forecast System (https://www.ecmwf.int/en/forecasts). We have used forecasts providing temperature and pressure

profiles in correspondence of 91 model levels on a $0.1° \times 0.1°$ grid. The vertical resolution increases linearly starting from 20-30 m up to about 400 m below 6 km allowing quite accurate determination of the ABLH. Moreover, the forecast time resolution of 1 h ensuring the calculation of sufficient number of ABLH reference points for all the considered Potenza cases. The ABLH reference points for the Evora 72h exercise dataset has been calculated using the forecasts provided by Global Data Assimilation System (GDAS) of the National Centers of Environmental Predictions of NOAA (https://www.ready.noaa.gov/gdas1.php). In this case the atmospheric temperature and pressure profiles are given for 23 model levels on a $1° \times 1°$ grid. The vertical resolution increases with the altitude starting from values of 200-300 m close to ground and reaching values of about 800 m at around 6 km. The forecast time resolution is 3 h. We used GDAS forecasts to calculate the ABLH reference for 72h Evora dataset because we do not have access to the corresponding ECMWF NWP. Both ECMWF and GDAS forecasts have been obtained through the CloudNET data portal (http://devcloudnet.fmi.fi).

4.1 EARLINET 72h Exercise

Fig. ?? shows the total attenuated backscatter time series at 1064 nm measured by the MUSA system during the 72h EAR-LINET exercise (????). The lidar observations started on July 9, 2012 at 08:00UTC and went on almost continuously until July 12, 2012 08:00UTC. The aerosol load observed during these measurements is consistent with a typical summer day in Potenza. The aerosol aloft is mainly dust while the layer at surface (into the ABL) is typically composed by local aerosols mixed with dust. Often, the aerosols in the free troposphere tend to intrude in the ABL making the separation between the ABL and the upper atmospheric region not so clear. This is clearly visible around noon on 10 July and 11 July 2012. The general idea behind the retrieval of ABLH from lidar measurements is to use the aerosol as tracers of the ABL and assuming that the ABLH is given by the top of the first aerosol layer (starting from the surface). According to this assumption, we can clearly see that the ABLH is maximum around noon (when the solar convection is at its maximum) for all the three days and it reaches its minimum during nighttime. The black line in Fig. ?? shows the ABLH as retrieved by MIPA algorithm. In general, the expected temporal evolution of the ABLH is well captured and the intrusions of the upper aerosol layers in the ABL do not seem to affect the outcomes, thus still obtaining reasonable ABLH estimates.

It is important to highlight that the assumption to retrieve the ABLH as the top of the first detected aerosol layer is valid only if the ABL is above the full lidar overlap height. During nighttime observations, this condition may be not always verified and in this case the algorithm detects as first edge the base of the layer next to the ABL top. This is clearly visible during the nighttime period in Fig. ?? where the real ABL is too low to be detected with the MUSA system and the retrieved ABLH is typically overestimated (?).

As explained in Sect. ??, the MIPA algorithm is composed by four different modules: an edge detector based on Canny filter (see Sect. ??), a module for reducing the vertical resolution (see Sect. ??), the pre-processing module described in Sect. ?? to be applied before the edge detector and, finally, a post-processing (see Sect. ??) to be applied after the edge detector step. Fig. ?? shows the role played by each of these modules in retrieving the ABLH for the Potenza 72h dataset and also the reference ABLH retrieved using the ECMWF forecasts (brown circles). The ABLHs shown in the upper panel of Fig. ?? were calculated considering the different steps of the MIPA algorithm, i.e. applying: the edge detector module on full resolution data (curve

a in upper panel of Fig. **??**), the vertical resolution reduction module and the edge detector (curve *b*), the vertical resolution reduction module, the pre-processing module and the edge detector (curve *c*) and finally the whole algorithm (curve *d*). It is

390 evident that the edge detector is not sufficient to ensure a stable retrieval even if it is applied to a reduced resolution dataset. Consequently, the application of the post-processing module is crucial in the processing. The absolute differences with respect to the reference are plotted in bottom panel of the Fig. **??**. In calculating the absolute difference, the reference data have been always interpolated at the same resolution of the lidar data assuming that the ABL is slowly varying.

The upper panel of Fig. **??** shows the comparison between the ABLH retrieved by the MIPA algorithm and the corresponding

395 one obtained by using more traditional ABLH detection approaches. Specifically, we applied to the same dataset different algorithms for the ABLH estimation: the MIPA algorithm **??**, the derivative method described in Sect. **??** and the procedure based on WCT as in Sect. **??**. The ABLH retrieved using the ECMWF forecasts is reported as brown circles in Fig. **??**. The agreement among the ABLH obtained by applying the considered algorithms on lidar data is satisfactory. The MIPA algorithm provides the smallest discrepancies with respect to the reference. In general all the algorithms overestimate the ABLH in

400 nighttime conditions. As already mentioned earlier, this discrepancy can be due to two main reasons: the first one is related to the different definitions we adopted to retrieve the ABLH (the ABLH reference points are based on a thermodynamic definition of the ABL, while the ABLHs retrieved from lidar observations use the atmospheric aerosol as proxy to characterize the ABL); the second reason is due to the fact that the ABLH as retrieved by ECMWF forecasts data may be below the full overlap of the MUSA lidar.

405 The absolute difference of all the considered algorithms with respect to the reference is plotted in the bottom panel of Fig. **??** and a statistical analysis is reported in Tab. **??** for all the considered algorithms. Both Fig. **??** and Tab. **??** confirm the better performance of the MIPA algorithm with respect to the other approaches into the proposed benchmark.

Fig. **??** reports the lidar observations at 1064 nm made by PAOLI over the Evora site during the 72h EARLINET exercise. Differently from Potenza, there are not lofted aerosol layers in the atmosphere and most of the aerosol load is trapped in the

410 ABL. The typical evolution of the ABL due to solar activity is clearly visible in the plot. Moreover, sometime there are small convective clouds formed on the top of ABL (see for example around 6:00 UTC of July 11). The MIPA algorithm captures quite well the evolution of the ABLH (black line in Fig. **??**).

Fig. **??** is similar to Fig. **??** but refering to the 72h Evora dataset. The only difference with respect to Potenza 72h dataset is that, in this case, the reference is calculated exploiting atmospheric temperature and pressure profiles provided by the GDAS

415 forecasts.

Tab. **??** sums up the statistical analysis of the absolute differences with respect to the reference for all the considered algorithms for the 72h Evora dataset. As for Potenza, the better performance is the one corresponding to the proposed ABLH retrieval algorithm. It is worth to be underlined that during daytime there is quite a good agreement between the GDAS forecasts and the outcomes of the MIPA approach, instead, during nighttime, the MIPA retrievals may be hindered by PAOLI's overlap

420 for low ABLHs or overestimated in all the cases where in the ABL there is a residual layer higher than the stable layer.

4.2 Other Potenza Cases

In this section we describe three additional case studies on which the proposed MIPA algorithm has been evaluated. The three cases refer all to MUSA lidar observations during three longer continuous observations ever made over Potenza with MUSA.

The first case study refers to April 21, 2010 when the Potenza EARLINET station performed a quite long record of lidar measurement concurrently with the eruption of the Icelandic volcano Eyjafjallajökull occurred in April-May 2010. During the eruption almost all the EARLINET stations promptly started continuous measurements, whenever weather conditions allowed it and the corresponding outcomes are described by (**?**).

Fig. **??** shows the comparison between the ABLH retrieved by the MIPA algorithm and the corresponding ABLH obtained by using the other considered algorithms (upper panel). ABLHs retrieved from ECMWF runs are assumed as reference (brown circles). The absolute difference of all the considered algorithms with respect to the reference is plotted in the bottom panel of Fig. **??**. For this case, from 08:30UTC to 17:00UTC, all the considered lidar retrieval algorithms give ABLH values systematically below the reference ones. This behavior can be explained looking at Fig. **??**, where the total attenuated backscatter time series at 1064 nm measured by the MUSA system on April 21, 2010 is shown. Moreover, the black line shows the ABLH retrieved by MIPA and the white line shows the reference ABLH. Before the 8:30UTC the real ABLH is below the MUSA overlap and, consequently, as already mentioned earlier, the proposed algorithm overestimates the ABLH capturing the edge of the next layer. Starting from the 08:30UTC, the solar activity initiates and the ABLH starts to increase above altitudes exceeding the lidar overlap. Thus, from this point on, the ABLH retrieved by using lidar measurements should agree with the reference one. However, in this particular case, the lidar observations show that two separated aerosol layers are present below the reference ABLH (about 3 km asl) indicating probably a not well mixed ABL. The bottom layer (below about 1.5-2.0 km asl) is probably composed by local particles while the upper one contains dust of mixed dust. Clearly, in conditions like this, the ABLH retrieved by lidar measurements (independently from the specific algorithm) will underestimate the real ABLH capturing the top of the first aerosol layer and not the top of the ABL.

The other two cases refer to nighttime observations taken on Nov 20, 2014 and July 13, 2015. Figs. **??** and **??** report the comparison of PBHL retrieved by all the considered algorithms (upper panel) and the absolute differences with respect to the reference (bottom panel) for the selected cases, respectively.

The agreement among all the considered algorithms is in general good for all the three cases. For all the cases in the dataset, MIPA algorithm shows the highest accuracy with respect to the reference. This is confirmed also by the mean and median values of the absolute difference with respect to the reference summarized in Tab. **??** (minimum values of both these parameters are always obtained by using the proposed algorithm).

5   Conclusions

The estimation of the ABLH is of crucial importance both for meteorological and air-pollution related applications. In this work, we proposed a new algorithm to continuously retrieve the ABLH. This approach leverages on the use of a fully image-based methodology (instead of analyzing the lidar observations profile by profile). The retrieval consists in applying to the

image, during the pre-processing phase, morphological operators. Afterwards, an edge detection is considered. Finally, during the post-processing phase, the significant edges are extracted through a further filtering phase based on mathematical morphology and an object-based analysis. This approach has been compared with a proper benchmark consisting of state-of-the-art ABLH estimation methods, i.e., a gradient-based approach and a WCT-based method. For the latter, the filtering capabilities of the approach were pointed out. Different datasets acquired by two lidar systems located in two separated EARLINET permanent observational sites have been considered to assess the performance.

The results, relying upon several statistical indexes, put in evidence that the proposed approach is more accurate than the compared approaches belonging to the benchmark. In particular, we observed an improvement of the accuracy of about 30% (on average) with respect to the closest state-of-the-art approach (i.e., the WCT). Moreover, the outcomes obtained by the MIPA are more stable than the other benchmarking methods. This can be easily pointed out by having a look at the results depicted in this paper and it has also been corroborated by calculating measures of dispersion (e.g., the standard deviation) in the statistical analysis. The last concluding remark is about the computation analysis. Despite of the proposed approach seems quite complex, it leverages on the use of very efficient filters based on mathematical morphology. The running times on large datasets (72 hours) show excellent performance from this point of view requiring just few seconds for the execution of the whole signal processing chain. The bottleneck of the system turns out to be the object analysis phase. However, the computation times can be considered comparable with the other approaches proposed into the benchmark.

Finally, it is worth to be stressed that the MIPA approach does not depend on the absolute calibrated values but rather only on the correlation among adjacent lidar range bins, which is of crucial importance in order to form the image. This interesting feature could be very useful for future developments. Indeed, the MIPA approach could be easily adapted to address the task of the estimation of the ABLH using other widely available and continuously acquired data, such as, ceilometer data.

Author contributions. Conceptualization, G.V. and S.L.; methodology, G.V.; software, G.V. and D.S.; validation, G.V., G.D.A., and D.S.; formal analysis, G.V.; data curation, G.D.A., A.A., and D.B.; writing–original draft preparation, G.V., G.D.A., D.S., S.L.; writing–review and editing, A.A., D.B., and G.P.; supervision, G.D.A. and G.P.; project administration, G.P.; funding acquisition, G.P.

Competing interests. The authors declare that they have no conflict of interest.

Acknowledgements. ACTRIS (www.actris.eu) has received funding from the European Union's Horizon 2020 research and innovation programme under grant agreement numbers: 654109 (ACTRIS-2), 759530 (ACTRIS-PPP), 871115 (ACTRIS-IMP), 824068 (ENVRI-FAIR), and previously from the European Union Seventh Framework Programme (FP7/2007-2013) under grant agreement n° 262254. The Portuguese lidar station is also supported by national funds through FCT—Foundation for Science and Technology, I.P., within the scope of the projects UIDB/04683/2020 e UIDP/04683/2020 and also through project TOMAQAPA (PTDC/CTAMET/29678/2017). Moreover, the

authors gratefully acknowledge CloudNET for providing ECWMF and GDAS atmospheric forecasts for all the measurement cases included in this study.
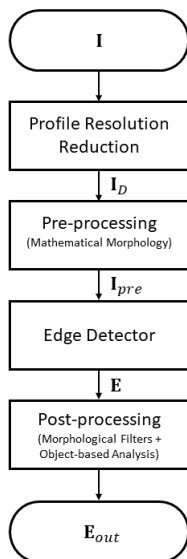
Figure 1. The flowchart of the MIPA algorithm.
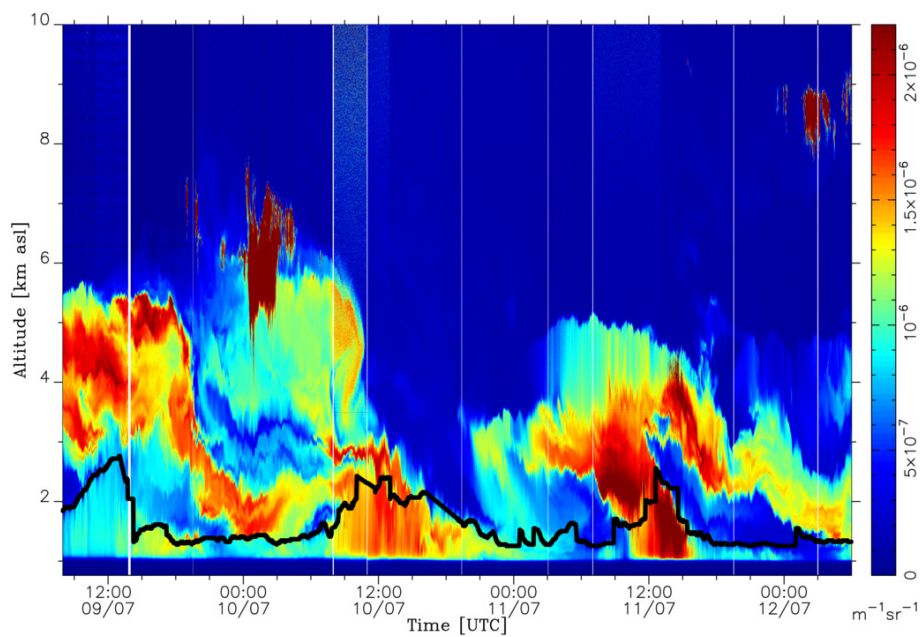
Figure 2. High-resolution time series of the total attenuated backscatter at 1064 nm measured over Potenza during the EARLINET 72h exercise (July 9-12, 2012). Time resolution is 60 s, vertical resolution is 3.75 m. The black curve shows the ABLH as retrieved by the proposed MIPA algorithm.

Table 1. Parameter setting for the WCT and MIPA approaches. The values of the parameters can be different for different lidar systems. Thus, they are reported for both MUSA (Potenza) and PAOLI (Evora) lidar systems.

Parameter	MUSA	PAOLI
WCT		
a	46	16
MIPA		
R	6	1
l_{pre}	3	6
l_{post}	6	6
θ_{min}	-66°	-46°
θ_{max}	66°	46°
δ_{post}	10	10

Table 2. Statistical analysis of the absolute differences with respect to the reference of the ABLH retrieved by applying MIPA, WCT and derivative approaches on Potenza 72h high-resolution time series of the total attenuated backscatter at 1064 nm. The mean (Δ_{mean}), the median (Δ_{mean}), the standard deviation (Δ_{std}), the standard error (Δ_{ste}), the minimum and the maximum of the absolute differences are given in meters. N is the number of points on which the statistics are made. The reference is assumed to be the ABLH calculated from the co-located atmospheric temperature and pressure profiles provided by ECMWF forecasts.

	MIPA	WCT	Derivative
Δ_{mean}	455	620	694
Δ_{med}	499	540	631
Δ_{std}	218	376	450
Δ_{ste}	26	45	54
Δ_{min}	25	62	21
Δ_{max}	875	1769	1719
N	69	69	69
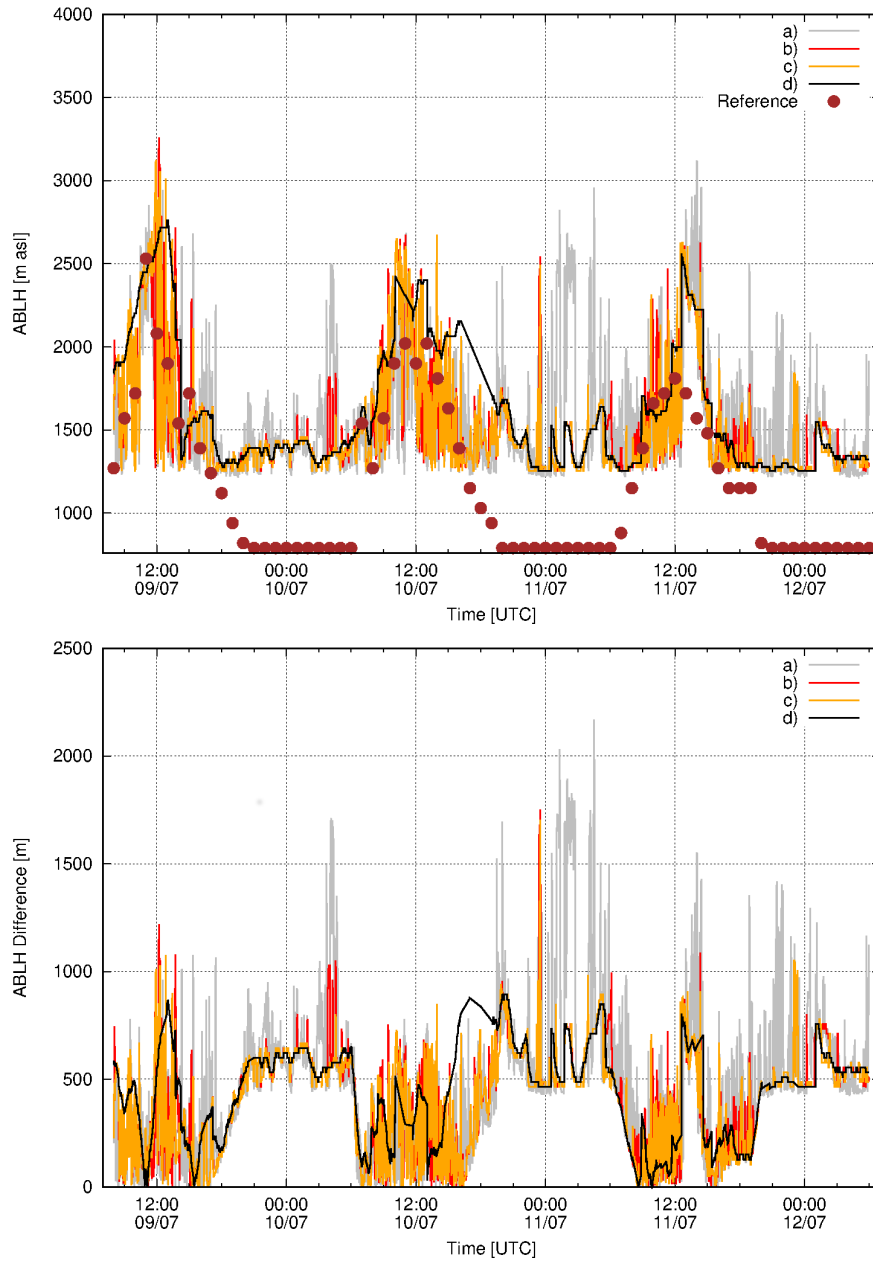
Figure 3. Upper panel: ABLH retrieved during the 72h EARLINET exercise (July 9-12, 2012) for Potenza. Gray, red, yellow and black lines show the ABLH retrieved from 1064 nm high-resolution total attenuated backscatter time series by applying the edge detector module on full resolution data (curve *a*), the vertical resolution reduction module and the edge detector (curve *b*), the vertical resolution reduction module, the pre-processing module and the edge detector (curve *c*) and the whole MIPA procedure (curve *d*). Brown circles are the reference ABLHs as retrieved from atmospheric temperature and pressure profiles provided by ECMWF forecasts. Bottom panel: Absolute differences of the retrieved ABLHs with respect to the reference. The original time resolution of ECMWF forecasts is 1 hour. They have been interpolated at the lidar data time resolution (60 s).
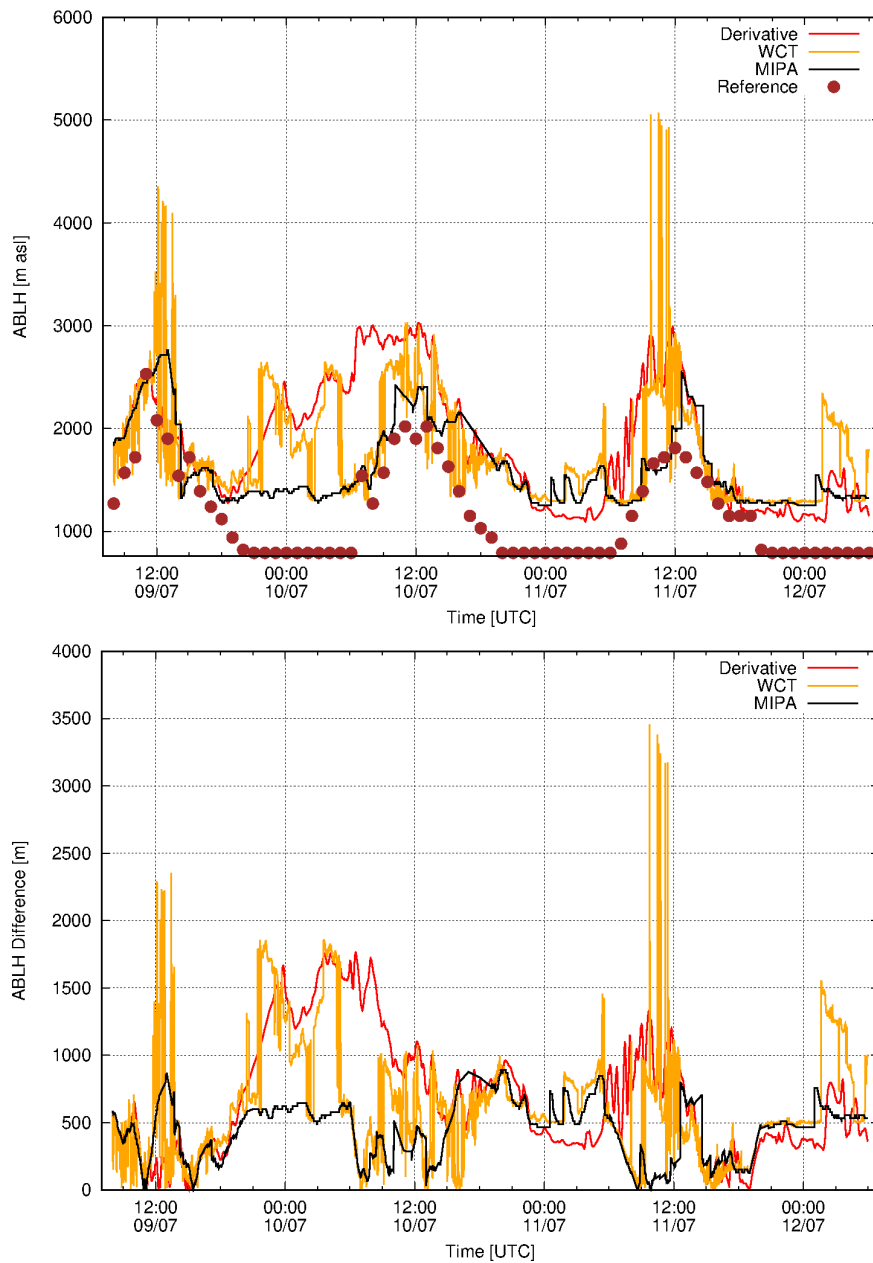
Figure 4. Upper panel: ABLH retrieved during the 72h EARLINET exercise (July 9-12, 2012) for Potenza. Black, red and yellow lines show the ABLH retrieved from 1064 nm high-resolution total attenuated backscatter time series applying MIPA, derivative and WCT algorithms, respectively. Brown circles are the reference ABLH as retrieved from atmospheric temperature and pressure profiles provided by ECMWF forecasts. Bottom panel: Absolute differences of the retrieved ABLHs with respect to the reference. The original time resolution of ECMWF forecasts data is 1 hour. They have been interpolated at the lidar data time resolution (60 s).
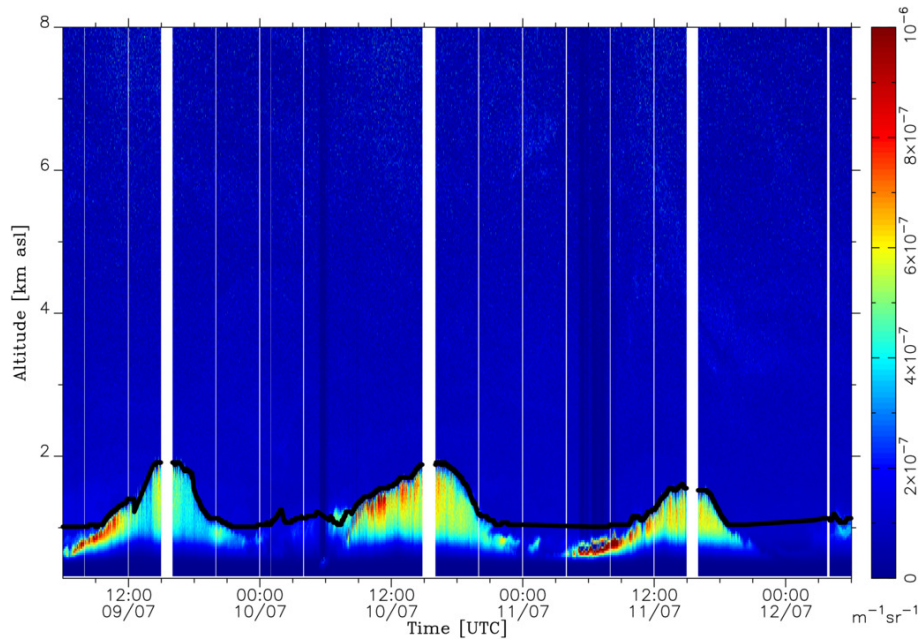
Figure 5. High-resolution time series of the total attenuated backscatter at 1064 nm measured over Evora during the EARLINET 72h exercise (July 9-12, 2012). Time resolution is 30 s, vertical resolution is 30 m. The black curve shows the ABLH as retrieved by the MIPA algorithm.

Table 3. Statistical analysis of the absolute differences with respect to the reference of the ABLH retrieved by applying MIPA, WCT and derivative approaches on Evora 72h high-resolution time series of the total attenuated backscatter at 1064 nm. The mean (Δ_{mean}), the median (Δ_{mean}), the standard deviation (Δ_{std}), the standard error (Δ_{ste}), the minimum and the maximum of the absolute differences are given in meters. N is the number of points on which the statistics are made. The reference is assumed to be the ABLH calculated from the co-located atmospheric temperature and pressure profiles provided by GDAS forecasts.

	MIPA	WCT	Derivative
Δ_{mean}	486	615	702
Δ_{med}	474	603	751
Δ_{std}	234	309	361
Δ_{ste}	49	64	75
Δ_{min}	80	78	159
Δ_{max}	962	1282	1455
N	23	23	23
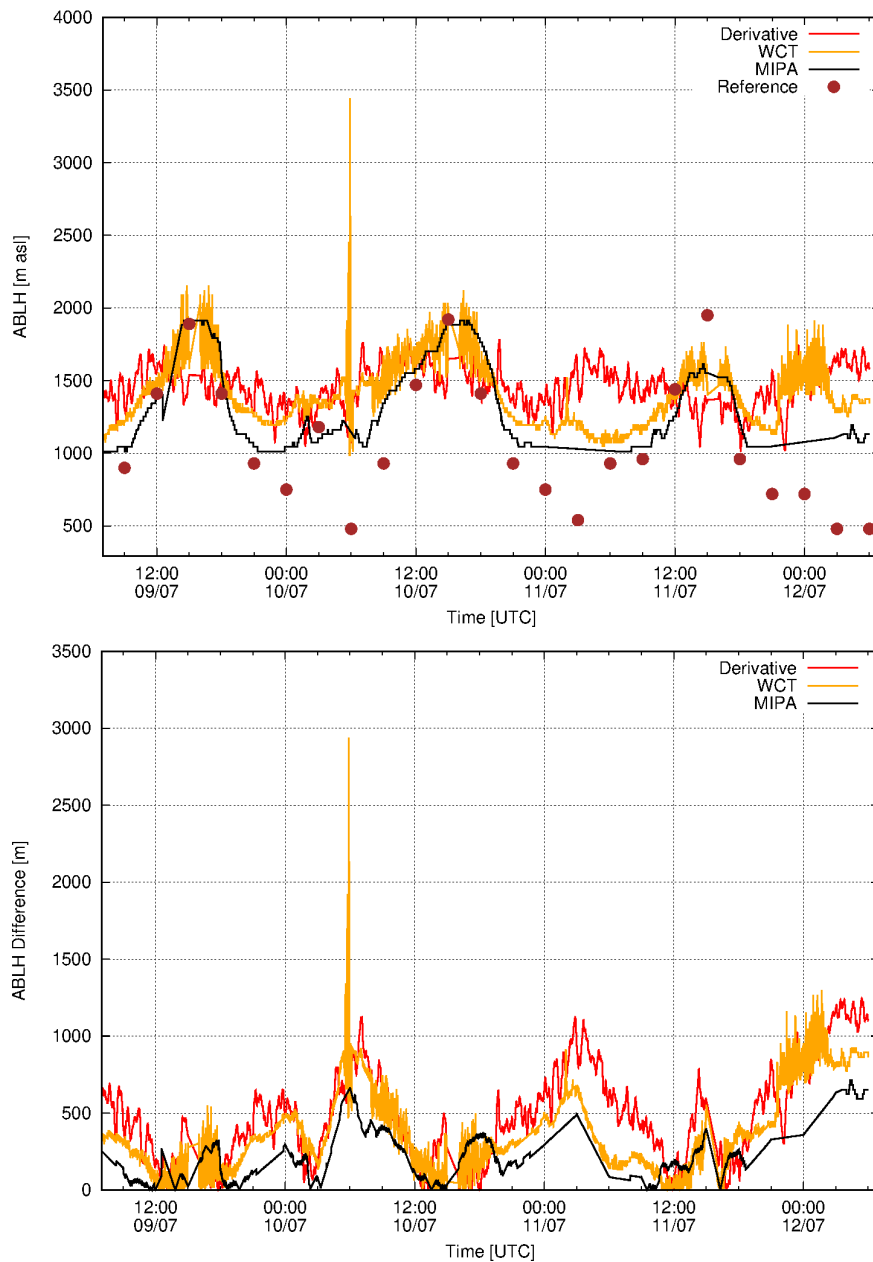
Figure 6. Upper panel: ABLH retrieved during the 72h EARLINET exercise (July 9-12, 2012) for Evora. Black, red and yellow lines show the ABLH retrieved from 1064 nm high-resolution total attenuated backscatter time series applying MIPA, derivative and WCT algorithms, respectively. Brown circles are the reference ABLHs retrieved from atmospheric temperature and pressure profiles provided by GDAS forecasts. Bottom panel: Absolute differences of the retrieved ABLHs withe respect to the reference. The original time resolution of GDAS forecasts data is 3 hour. They have been interpolated at the lidar data time resolution (30 s).
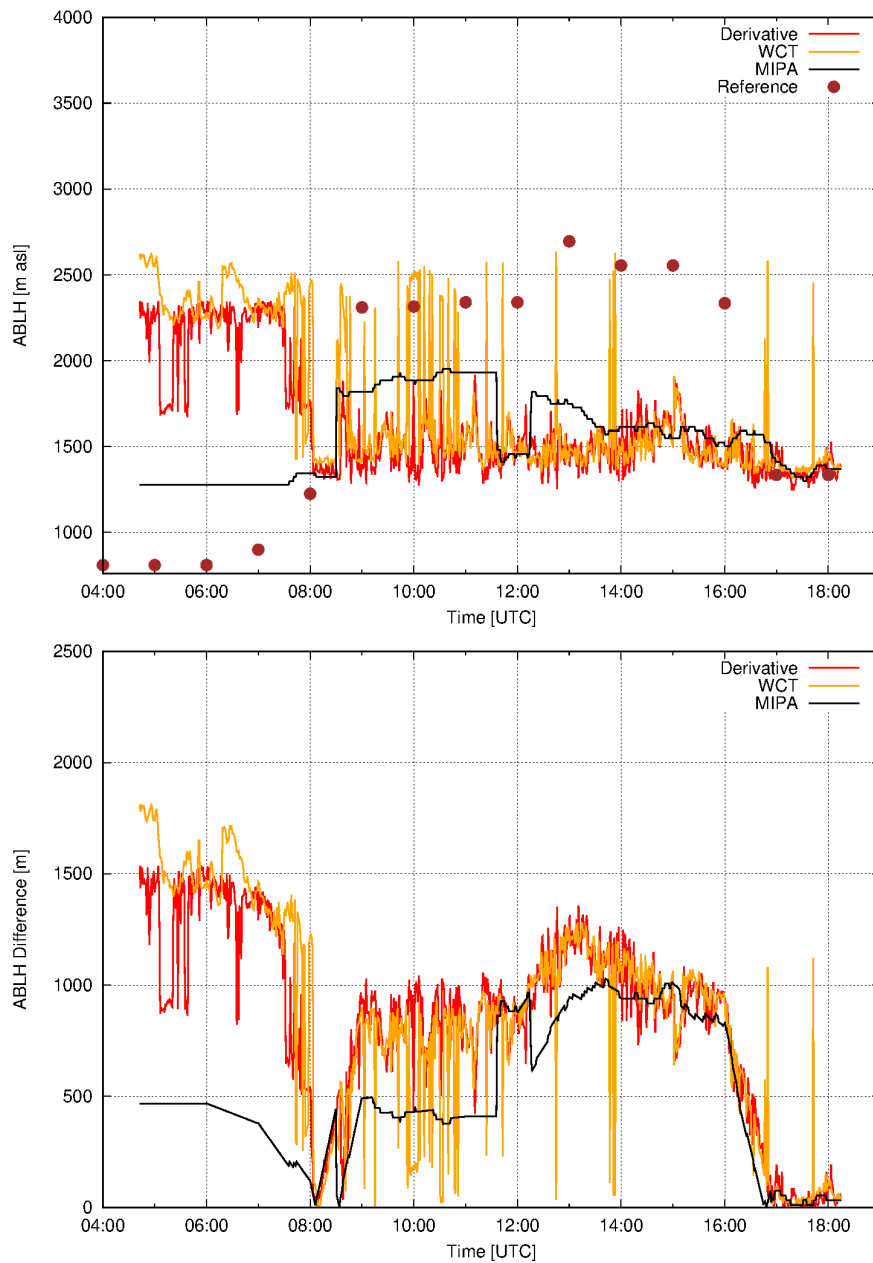
Figure 7. Upper panel: ABLH retrieved from the Potenza lidar measurements on April 21, 2010. Black, red and yellow lines show the ABLH retrieved from 1064 nm high-resolution total attenuated backscatter time series applying MIPA algorithm, derivative and WCT algorithms, respectively. Brown circles represent the reference ABLHs as retrieved from atmospheric temperature and pressure profiles provided by ECMWF forecasts. Bottom panel: Absolute differences of the retrieved ABLHs with respect to the reference. The original time resolution of ECMWF forecasts data is 1 hour. They have been interpolated at the lidar data time resolution (60 s).
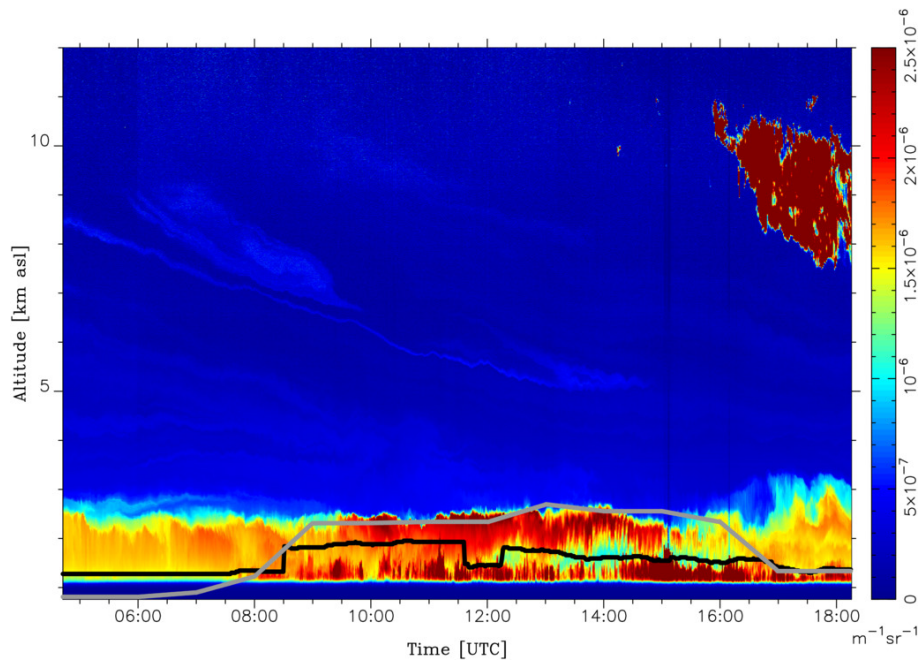
Figure 8. High-resolution time series of total attenuated backscatter at 1064 nm measured over Potenza on April 21, 2010. Time resolution is 60 s, vertical resolution is 3.75 m. The black and white curve shows the ABLH as retrieved by MIPA algorithm and by using ECWMF forecasts, respectively.
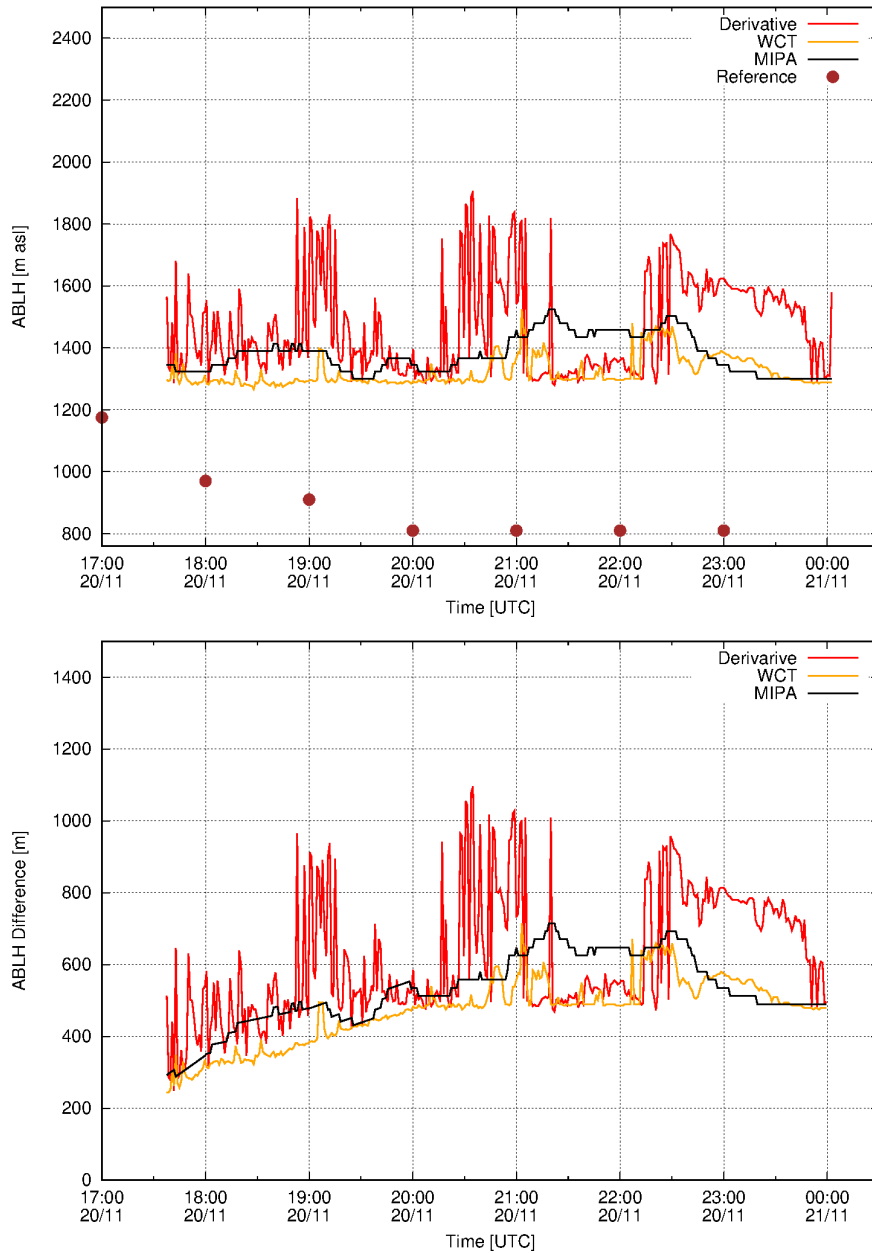
Figure 9. Upper panel: ABLH retrieved from the Potenza lidar measurements on November 20, 2014. Black, red and yellow lines show the ABLH retrieved from 1064 nm high-resolution total attenuated backscatter time series applying MIPA, derivative and WCT algorithms, respectively. Brown circles are the reference ABLHs as retrieved from atmospheric temperature and pressure profiles provided by ECMWF forecasts. Bottom panel: Absolute differences between the retrived ABLHs with respect to the reference. The original time resolution of ECMWF forecasts data is 1 hour. They have been interpolated at the lidar data time resolution (60 s).

Figure 10. Upper panel: ABLH retrieved from the Potenza lidar measurements on July 13, 2015. Black, red and yellow lines show the ABLH retrieved from 1064 nm high-resolution total attenuated backscatter time series applying MIPA, derivative and WCT algorithms, respectively. Brown circles are the reference ABLHs as retrieved from atmospheric temperature and pressure profiles provided by ECMWF forecasts. Bottom panel: Absolute differences between the retrieved ABLHs with respect to the reference. The original time resolution of ECMWF forecasts data is 1 hour. They have been interpolated at the lidar data time resolution (60 s).

Table 4. Statistical analysis of the absolute differences with respect to the reference of the ABLH retrieved by applying MIPA, WCT and derivative approaches on Potenza high-resolution time series of the total attenuated backscatter at 1064 nm in the 3 selected cases study (April 21, 2010, November 20, 2014, July 13, 2015). The mean (Δ_{mean}), the median (Δ_{mean}), the standard deviation (Δ_{std}), the standard error (Δ_{ste}), the minimum and the maximum of the absolute differences are given in meters. N is the number of points on which the statistics are made. The reference is assumed to be the ABLH calculated from the co-located atmospheric temperature and pressure profiles provided by ECMWF forecasts.

	MIPA	WCT	Derivative
2010-04-21			
Δ_{mean}	519	868	850
Δ_{med}	385	871	864
Δ_{std}	321	478	439
Δ_{ste}	84	128	117
Δ_{min}	24	83	26
Δ_{max}	963	1613	1420
N	14	14	14
2014-11-20			
Δ_{mean}	531	470	610
Δ_{med}	543	508	578
Δ_{std}	100	93	119
Δ_{ste}	41	38	49
Δ_{min}	378	325	450
Δ_{max}	645	552	790
N	6	6	6
2015-07-13			
Δ_{mean}	466	829	614
Δ_{med}	452	928	500
Δ_{std}	35	275	236
Δ_{ste}	13	104	89
Δ_{min}	437	406	405
Δ_{max}	540	1125	947
N	7	7	7